Chapter 23

Downburst monitoring and prediction studies

Kenneth L. Pryor
NOAA/NESDIS Center for Satellite Applications and Research (STAR), College Park, MD, United States

Chapter outline

And suddenly a sound came from heaven like the rush of a mighty wind, and it filled all the house where they were sitting.

Acts 2:2 Revised Standard Version Bible

1. Introduction

Downbursts are strong downdrafts that induce an outburst of damaging winds at or near the ground, and a microburst as a very small downburst with an outflow diameter of less than 4 km and a lifetime of less than 5 min (Fujita, 1985; Wakimoto, 1985). The dangers posed by convective storm-generated downbursts have been extensively documented. Since 2000, the National Transportation Safety Board (NTSB) has recorded 48 downburst-related accidents over CONUS with 42 fatalities (National Transportation Safety Board 2021) that involved personal or instructional aircraft. Severe windstorms (i.e., widespread convective wind gusts $>25.7\,\mathrm{m\,s^{-1}}$ (50 kt)) resulting from mesoscale convective systems (MCS) cause significant disruption to society, including widespread power outages, tree and structural damage, and transportation accidents that affect multistate regions and metropolitan areas along their track. Among them, a derecho, defined as a long-lived, widespread severe convective windstorm, is composed of numerous downbursts that are organized into clusters or families of clusters. Derechos can produce winds above hurricane force along a track that may exceed several hundred (~400) kilometers. Between 1987 and 2002, severe convective windstorms resulted in a total property loss of over $3 billion in the United States, with an average loss per event of $96 million. Also, between 1986 and 2003, severe convective windstorms were responsible for a total of 153 deaths and 2605 injuries, proving to be more deadly and hazardous than the low-end (F-0/F-1 intensity) tornado outbreaks that occurred during the same period and resulted in only 71 deaths (Ashley and Mote, 2005). Because these events are severe, it is important to understand the factors that lead to the downbursts and utilize all available observations to monitor and forecast their development.

Proctor (1989) and Pryor (2015) noted that convective windstorm potential has been traditionally expressed as a grouping of stability parameters relevant for downburst generation. These include the lower-to-mid-tropospheric temperature and equivalent potential temperature (theta-e) lapse rates, vertical relative humidity differences, and the amount of convective available potential energy (CAPE) in the troposphere. Some factors increase the likelihood of severe convective winds, which are (1) an elevated mixed layer that promotes instability by generating powerful storm updrafts and downdrafts (Banacos and Ekster, 2010) and (2) a rear-inflow jet into an MCS (Smull and Houze Jr., 1987; Weisman, 1992) which channels unsaturated mid-tropospheric air into the leading convective storm line. The establishment of an elevated, ascending front-to-rear flow originating from deep, moist convection, overlying a strong and deep outflow-induced cold pool has been found to generate and sustain a robust rear inflow jet (Weisman, 1992). Other factors documented by Proctor

Field Measurements for Passive Environmental Remote Sensing. https://doi.org/10.1016/B978-0-12-823953-7.00024-1

(1989) and Srivastava (1985) can reduce the likelihood of severe convective winds, such as the presence of a lower-tropospheric temperature inversion and a surface-based layer of unsaturated air that reduces virtual temperature.

Meteorological satellite measurement data, especially brightness temperature measured at the surface and convective cloud tops, have been previously exploited to study the troposphere's thermodynamic structure and convective storms' physical structure. Fujita and Wakimoto ("FW," 1981) demonstrated one of the earliest studies that identified infrared imagery from geostationary satellites showing definite cloud-top signatures associated with large and robust downbursts on the ground. Ellrod (1989) first applied geostationary sounder instrument data to the study of downburst potential assessment for the August 2, 1985, Dallas-Ft. Worth (DFW), Texas microburst storm. Since then, new technology and instrumentation have improved monitoring severe windstorms.

This chapter presents a discussion of the science of operational forecasting of severe windstorms through examples of employing new satellite and ground-based microwave and vertical wind profile data. Accordingly, this chapter is organized as follows: Section 2 is a detailed background of severe convective windstorm theory that includes a discussion of windstorm genesis and evolution. Section 3 is a summary of instrumentation and measurement application methodology. Finally, as an example of the coordinated use of surface- and satellite-based observational instrumentation, Section 4 presents case studies of downburst events from local to regional scale. The objective of this instruction is to build a multistep procedure for operational convective storm downburst monitoring and prediction.

2. Theoretical background of severe convective windstorms: Genesis and evolution

The outline of convective windstorm theory begins with the requirement that severe storms are highly organized. Construction of a model of severe convective winds from a simplified vertical momentum equation is derived from Newton's 2nd Law and expressed in Eqs. (1a), (1b):

$$a = F/m = (-1/\rho)(dp/dz) + g\left(T_{ve} - T_{vp}\right)/T_{ve} \tag{1a}$$

$$a = F/m = (-1/\rho)(dp/dz) + g\left(\rho_o - \rho_f\right)/\rho_o \tag{1b}$$

where a is the acceleration, ρ is the density of the medium, p is the pressure, z is the altitude in the atmosphere, and T_{ve} and T_{vp} are virtual temperatures of the environment (atmosphere) and the parcel, respectively.

Downdraft initiation proceeds as a departure from hydrostatic equilibrium. For a volume of air with a high concentration of ice phase precipitation that develops within a convective storm, the resultant force F on the precipitation volume is downward and imparts negative buoyancy. This physical basis can be extended to more complex convective systems in which updrafts, downdrafts, and outflow foster a rear inflow jet's development.

The standard NOAA/National Weather Service (NWS) definition of a severe thunderstorm includes damaging winds with gusts of $26\,\mathrm{m\,s^{-1}}$ (50 kt) or greater and hail with a diameter of 2.5 cm (1 in.) or greater. Severe thunderstorms are most identifiable in weather radar imagery, in which a large concentration of ice-phase precipitation within a volume results in high reflectivity resulting from increased backscattering. Downdraft severity is governed by phase change and the loading of ice-phase precipitation. Loading, in effect, refers to the mass of a collection of hydrometeors. When gravity is imposed upon the volume of hydrometeors, downward acceleration occurs due to precipitation's weight.

Numerous studies through the 1980s and 1990s provided observational analyses and conceptual models for severe convective wind generation that addressed environmental and storm microphysical and dynamic attributes. A prototypical conceptual model of a deep moist convective (DMC) storm is shown in Fig. 1. Fujita and Wakimoto ("FW," 1981) noted that damaging winds induced by thunderstorms were classified into a tornado and straight-line winds and further identified a subclassification of straight-line winds into two categories: the downburst and the gust front. FW formulated the definition of the downburst as stated at the beginning of Section 1. This study identified that infrared imagery from geostationary satellites showed definite cloud-top signatures associated with large and strong downbursts on the ground.

Srivastava (1987) found that precipitation in the form of ice increases the convective downdraft intensity. This effect increases with precipitation content and the stability of the environmental lapse rate of temperature. The power of the downdraft also increases in proportion to the relative concentration of smaller particles. Condensate loading (Srivastava, 1987), sometimes combined with subsaturated air entrainment in the storm middle level (Knupp, 1989), initiates the convective downdraft. The subsequent melting of frozen hydrometeors and subcloud evaporation of liquid precipitation, in conjunction with precipitation loading, result in the cooling and negative buoyancy that accelerate the downdraft in the unsaturated layer (Srivastava, 1987). The melting of ice-phase precipitation, subsequent evaporative cooling, and the resulting downdraft strength are enhanced by sizeable liquid water content and the related water surface available for evaporation. A large

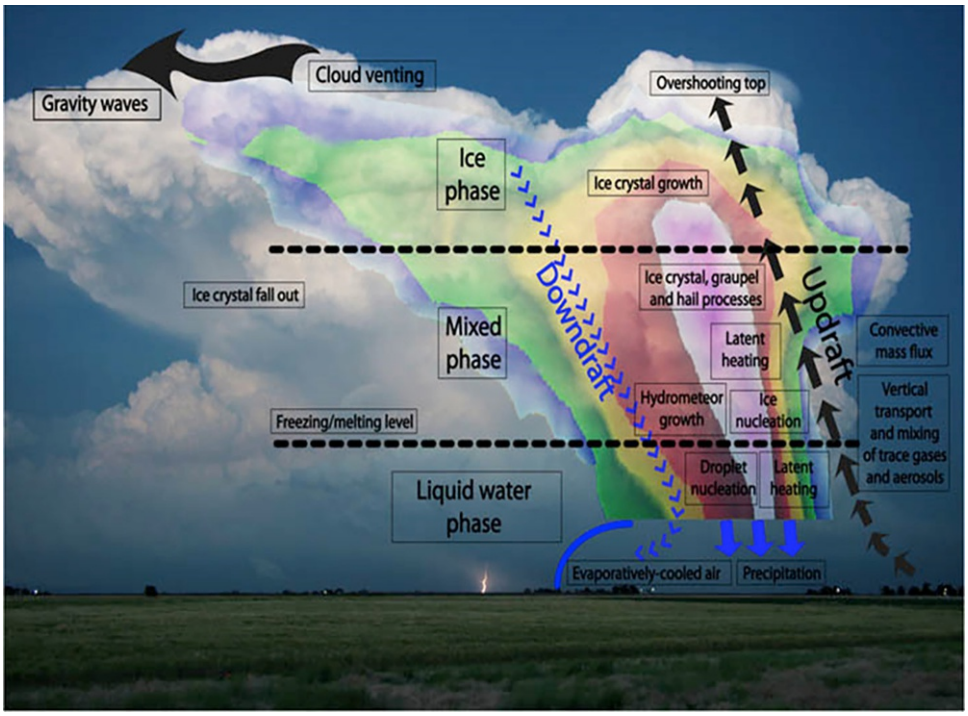

FIG. 1 Conceptual model of a deep convective storm with the potential to generate intense downdrafts and damaging downburst winds. *(Courtesy of Rob Seigel and Susan C. van den Heever, Global Precipitation Measurement (GPM, available online at https://gpm.nasa.gov/GPM, accessed on 7 July 2020)).*

lapse rate maintains negative buoyancy as the downdraft descends in the subcloud layer (Srivastava, 1987). As the lapse rate's stability is increased, higher precipitation contents, precipitation in the form of ice, and relatively higher concentrations of small precipitation particles are required to force an intense downdraft. At this point in the downdraft initiation process, potential energy resulting from temperature deficit between the precipitation-infused parcel and the ambient environment is converted to downward air parcel motion, which, collectively, comprises the convective downdraft. As the lapse rate becomes even more stable, only wet downbursts having substantial precipitation in the form of ice are possible. A downburst can be driven solely below the cloud base where melting and evaporation of precipitation and precipitation loading below the cloud base are sufficient to produce wet downbursts.

Knupp (1989, 1996) refined the understanding of the downburst generation's physical and dynamic processes. The author noted that low-level downdrafts are closely controlled by the arrival of precipitation at low levels. In the storm middle levels, air flows quasi-horizontally around the updraft flanks and converges into the downshear flank, referred to as the wake. Within the wake region, where entrainment reduces positive buoyancy and associated updraft strength, precipitation at middle levels (where it is grown most effectively) is then allowed to descend to lower levels. The intrusion of drier air into the wake's precipitation region also enhances the evaporation/sublimation process. Diabatic cooling from melting and evaporation is most effective at levels below the melting level. Convergence within the downshear wake is thus instrumental in transporting precipitation into the downshear flank. Therefore, a comprehensive understanding of the downdraft initiation process is closely related to the precipitation initiation and transport process within clouds and is observable in passive MW imagery, as shown in the following case studies. Such processes depend not only on vertical profiles of temperature and moisture but also on vertical environmental wind profiles. Knupp (1996) identified the protrusion echo produced by settling hydrometeors from a line of weak updraft that formed in association with low-level confluence located east of the storm core. The protrusion appears to be partly forced by existing mesoscale convergence, while the updraft within its lower levels represents the weak low-level ascent along the up-down downdraft branch. In this regard, the protrusion is indirectly connected to the strong core downdraft. Initial bowing of the echo (Przybylinski, 1995) is associated with the early microburst activity, a characteristic observed in other case studies. The inference of downburst occurrence can be successfully applied by the synergistic use of satellite-based passive MW and ground-based Doppler radar data and imagery.

From Weisman et al. (1988) as a departure point, Weisman (1992) explored the role of vertical wind shear and buoyancy in the generation of a rear inflow jet and visualized the associated conceptual model of this process. Weisman (1992) noted that rear inflow is generated in response to the development of an upshear-tilted updraft, as the horizontal buoyancy gradients along the back edge of the expanding system create a circulation that draws midlevel air in from the rear. The rear

inflow jet system can take two forms, descending or elevated. For a descending-jet system, the convective circulation is characterized by an updraft current that ascends gradually above a spreading surface cold pool, with light-to-moderate convective and stratiform rainfall extending well behind the leading edge of the cold pool. This structure is often associated with a decaying system. The gust-front lifting is not strong or deep enough to regenerate new convective cells, and the mesoscale circulation slowly weakens. However, for an elevated-jet system, the circulation is dominated by strong, erect updrafts along the leading edge of the surface cold pool, with the updraft current spreading rapidly rearward above 7–8 km above ground level. Moderate-to-heavy convective rainfall exists at the system's leading edge, with lighter rainfall extending to the rear. This structure tends to be longer lived than the descending-jet case, as the deeper gust-front lifting regularly regenerates strong convective cells. The rear-inflow jet represents a new, potentially significant horizontal vorticity source that must be included when diagnosing various circulation sources' relative importance. Specifically, a rear-inflow jet that descends and spreads along the surface is characterized by the same sign of horizontal vorticity generated by the cold pool, thereby accentuating the cold pool circulation.

In contrast to a descending jet, an elevated rear-inflow jet is characterized by the opposite sign of horizontal vorticity generated by the cold pool (up to jet level), thereby accentuating the ambient vertical shear effects. Since significant rear-inflow characteristically develops after the cold-pool circulation overwhelms the ambient shear, a surface jet's development reinforces the upshear-tilting process that tends to weaken the system. However, an elevated rear-inflow jet's development reverses this process, promoting powerful, upright convective cells along the cold pool's leading edge. Johns (1993) built on the basis established by previous observational and modeling studies of environmental conditions associated with the development and maintenance of bow echo-induced damaging winds, focused on parameters related to storm outflow and updraft strengths. Specifically, wind speeds and relative humidity values in the mid-levels (related to outflow strength) and instability (related to updraft strength) were examined. The results indicated that these parameters exhibit a wide range of values when considering all bow echo situations in which damaging winds are reported. Further, combinations of wind speeds in the mid-levels and instability tend to vary with the season and the synoptic situation. For example, as detailed by Johns (1993) and Moller (2001), when powerful winds are present in the mid-levels, bow echo development has been observed in only marginally unstable environments. Bow echo events associated with the powerful wind-marginal instability combination typically occur with strong, rapidly moving low-pressure systems ("dynamic" synoptic pattern) in the colder months of the year. On the other hand, events associated with the relatively weak wind-extreme instability combination typically occur along a quasi-stationary thermal boundary in relatively stagnant weather regimes ("warm season" synoptic pattern) in the late spring or summer. Many bow echo wind events are associated with wind-instability combinations between the extremes. Some of these events are related to synoptic patterns that do not sufficiently match either prototypical pattern.

As will be demonstrated in the following case studies, passive microwave (MW) observations from polar-orbiting satellites are instrumental in identifying convective storms with dense ice-phase precipitation cores that can generate intense downdrafts by the processes of loading, melting, and evaporation. At a 12.5 km horizontal resolution, the 91 GHz channel on the Special Sensor Microwave Imager Sounder (SSMIS) effectively views the rainband structure in which both 91 GHz polarization (horizontal, "H" and vertical, "V") generate images where cirrus cloud decks are transparent. The SSMIS is a conical scanner with a 53.1 degrees zenith angle, swath width 1700 km, and scan rate of 31.9 scans/min, which equals 12.5 km/scan. Ferraro et al. (1998) introduced an expression to quantify brightness temperature derived from Schwarzchild's equation:

$$TB = T_u + \tau \cdot \left[\varepsilon \cdot T_s + (1 - \varepsilon) \cdot T_d\right] \tag{2}$$

where T_u is the upwelling atmospheric emission, τ is the transmittance, ε is the emissivity, T_s is the surface temperature, and T_d is the downwelling atmospheric emission. Scattering by large precipitation particles, especially by graupel, hail, and ice crystal aggregates (i.e., snow) above the freezing level, causes 91 GHz brightness temperatures (TB) to be low, referred to as a TB depression (Ferraro et al. (2015), Laviola et al. (2020)). Thus, convective rainbands tend to have very low TB, often below 200 K. Time trends in cloud top TB, as measured in MW spectrum window channels, and spatial patterns of cloud top TB, especially the geometry of TB gradients, can be exploited to infer downburst generation.

3. Field measurement application methodology

Surface-based measurements in the radio and microwave regions of the electromagnetic spectrum provide important environmental parameters for monitoring atmospheric stability and mesoscale and microphysical processes associated with convective storm development. Over CONUS, traditional data sets applied to both operational downburst monitoring

and prediction, as well as product validation, include surface-based observations of atmospheric parameters (i.e., temperature, humidity, wind speed/direction, sky condition, precipitation accumulation, etc.) from NWS/FAA aviation routine meteorological reports (METAR) stations, mesonetwork (mesonet) stations, radiosonde observations (RAOBs; see Chapter 2), and meteorological Doppler radar reflectivity and velocity measurements. The highest quality networks in CONUS include the Oklahoma Mesonet and West Texas Mesonet (Brock et al., 1995; Schroeder et al., 2005). These networks have a spatial density of weather stations suitable for observing patterns such as outflow boundaries and temperature perturbations resulting from convective storms. In effect, surface weather observation and analysis represent a primary important step in convective storm diagnosis process.

An ultra-high frequency (UHF) boundary layer profiler (BLP) is capable of identifying mesoscale features such as low-level jets, rear-inflow jets, and convective storm outflow and can supplement the Next Generation Weather Radar (NEXRAD) velocity azimuth display wind profile (VWP) product at longer distances (>30 km) from the adjacent NEXRAD site. The BLP is a Doppler radar system operating at a frequency of 915 MHz that provides high-resolution observations with enhanced sensitivity to hydrometeors (Ecklund et al., 1988) in which backscattered signals from turbulence-induced refractive index variations are detected by the radar (Martner et al., 1993). The BLP retrieves horizontal wind speed and direction up to an elevation of four kilometers above ground level at a vertical resolution of 60 m. In selected regions of CONUS, an expanded data set incorporates lower tropospheric vertical wind profile data. For example, in this chapter, we will utilize a BLP in Beltsville, Maryland (United States), which is near the capital, Washington, DC. The BLP at Howard University Beltsville Campus (HUBC) provides the most representative wind conditions in the Washington, DC metropolitan area. These BLPs are component of the Cooperative Agency Profilers (CAP) network, which compiles data in real-time, applies quality control, and distributes the data online. Current and archived BLP wind data are available on the CAP website: https://madis-data.ncep.noaa.gov/cap/

In addition, vertical temperature and moisture sounding data sets generated by the surface-based microwave radiometer profiler (MWRP) provide routine monitoring of thermodynamic patterns in both the preconvective and storm environments (Westwater et al., 2005). In the Washington, DC–Baltimore, Maryland corridor, the HUBC MWRP, manufactured by Radiometrics Corporation, observes atmospheric brightness temperatures in 12 frequency bands from 22 to 59 GHz and retrieves temperature and humidity soundings up to 10 km height with a vertical resolution of 50 m below 500 m AGL and a resolution of 100 m between 500 and 2000 m AGL. The MWRP exploits the 30 to 50 GHz transmission window to retrieve water vapor profiles, while exploiting the absorption band near 60 GHz for temperature sensing. In addition, the MWRP can obtain retrievals at zenith and a 15° elevation angle (Cimini et al., 2015). The HUBC MWRP employs the neural network (NN) inversion method of retrieval, as described in Cimini et al. (2015), trained with a large data set of profiles generated from historical data sets of operational radiosondes. Vertical temperature and humidity profiles are often applied to calculate CAPE, temperature lapse rates, and other atmospheric stability indices to determine the presence of conditional instability (CI) and potential instability. The parcel choice for CAPE computation is an important consideration. The most unstable parcel CAPE (MUCAPE) was selected due to its universality and versatility as an estimator of positive buoyancy for both elevated and surface-based convection (Bunkers and Klimowski, 2002), and thus applicable to the range of thermodynamic environments observed during the severe wind events. This chapter will demonstrate the thunderstorm downburst potential applications of the microburst windspeed potential index (MWPI, Pryor, 2015) as calculated from MWRP and satellite sounding data sets.

In the next section, we present two case studies, one for April 2020 in South Texas and another the June 2012 North American Derecho. These studies were selected because they (1) demonstrate the physical process of downburst generation described in Section 2 and they were (2) observed simultaneously by the microwave sensors onboard polar-orbiting meteorological satellites, vertical sounding profiles generated from the Infrared Atmospheric Sounding Interferometer (IASI) and the NOAA Unique Combined Atmospheric Processing System (NUCAPS), NEXRAD, and BLPs. NUCAPS (Nalli et al., 2020) is a NOAA enterprise algorithm that retrieves atmospheric profile environmental data records and is described in more detail in Chapters 14 and 18. The IASI instrument and its applications for vertical atmospheric sounding are also highlighted in Chapter 18. Data collection, processing, and visualization follow the methodology of Pryor (2015, 2017). We use microwave sensors on Meteorological Operational (METOP) and Defense Meteorological Satellite Program (DMSP) satellites. DMSP Special Sensor Microwave Imager Sounder (SSMIS) and METOP Microwave Humidity Sounder (MHS) 89–91 GHz window channel data sets were obtained from the NOAA Comprehensive Large Array-data Stewardship System (CLASS) and the EUMETSAT Data Centre, respectively. Dual-polarized 91 GHz brightness temperature data sets allow for the calculation of polarization-corrected temperature (Liu et al., 1995) as presented in the study of the April 2020 South Texas downburst case. Vertical temperature and wind profile data, up to 5 km above ground level, from the CAP network are applied to further study the favorable environment for severe convective storm winds.

The Next Generation Weather Radar (NEXRAD) level-II reflectivity and differential reflectivity factor ZDR are obtained from the National Center for Environmental Information (NCEI) and used to verify that observed wind gusts are associated with downbursts originating from high reflectivity factor storms and are not associated with other types of convective wind phenomena (i.e., gust fronts). Plan-view images of radar reflectivity and ZDR are constructed from the lowest elevation angle scan (0.46 degrees). An additional application of radar reflectivity factor imagery is to infer microscale physical properties of downburst-producing convective storms. Differential reflectivity factor is employed in case studies to analyze the vertical precipitation composition in convective storms and thereby indicate the presence of graupel and hail and discuss their role in the enhancement of convective downdrafts. Particular reflectivity signatures, such as bow echoes (Przybylinski, 1995) and protrusion echoes (Knupp, 1996), are effective indicators of downburst occurrence. Downburst occurrence can be further confirmed by calculating a surface ΔT value, where $\Delta T \equiv T(\text{downburst}) - T(\text{ambient})$ and represents the peak temperature departure from ambient at ground level (Proctor, 1989). ΔT can therefore serve as a proxy variable for the surface density perturbation through the ideal gas law. In summary, a comprehensive approach of observational data analysis involves both surface- and satellite-based instrumentation. Because this approach utilizes operational products available to weather service forecasters, it can feasibly be used for monitoring and forecasting downburst occurrence. Compared to other ground-based microwave imagery sources, such as Doppler radar, spatial patterns in TB can also infer airflow characteristics and circulation patterns surrounding the convective storm of interest.

4. Case studies of field measurement applications

4.1 27 April 2020 South Texas severe thunderstorm downbursts

A cluster of thunderstorms developed west of the dryline over the Davis Mountains of southwestern Texas during the afternoon of April 27, 2020, while a dryline extended from east of Midland, Texas to the Big Bend area as shown in the 2100 UTC surface analysis in Fig. 2. The thunderstorm cluster then merged to form an intense MCS with a leading bow echo (not shown) near the westward bulge in the dryline. As noted by Schaefer (1986) and Ziegler et al. (1997), the dryline is often a focus of differential heating, boundary layer convergence, and solenoidal circulation with an attendant release of instability and convective storm intensification. After dryline interaction, the MCS tracked rapidly southeastward toward the Gulf Coastal Plain. Fig. 3A shows a mid-afternoon (1946 UTC) NUCAPS physical retrieval sounding profile over Del Rio, Texas, which can be compared to a RAOB released from the same location 4 h later, at 0000 UTC on 28 April (Fig. 3B). The earlier NUCAPS Skew-T diagram (Fig. 3A) shows considerable CAPE (> 4000 J/kg), a large lower tropospheric temperature lapse rate (>9°C/km), and a prominent mid-tropospheric unsaturated layer. These features indicate an elevated probability of severe thunderstorm downburst occurrence, roughly 6 h before the onset of the severe windstorm. A

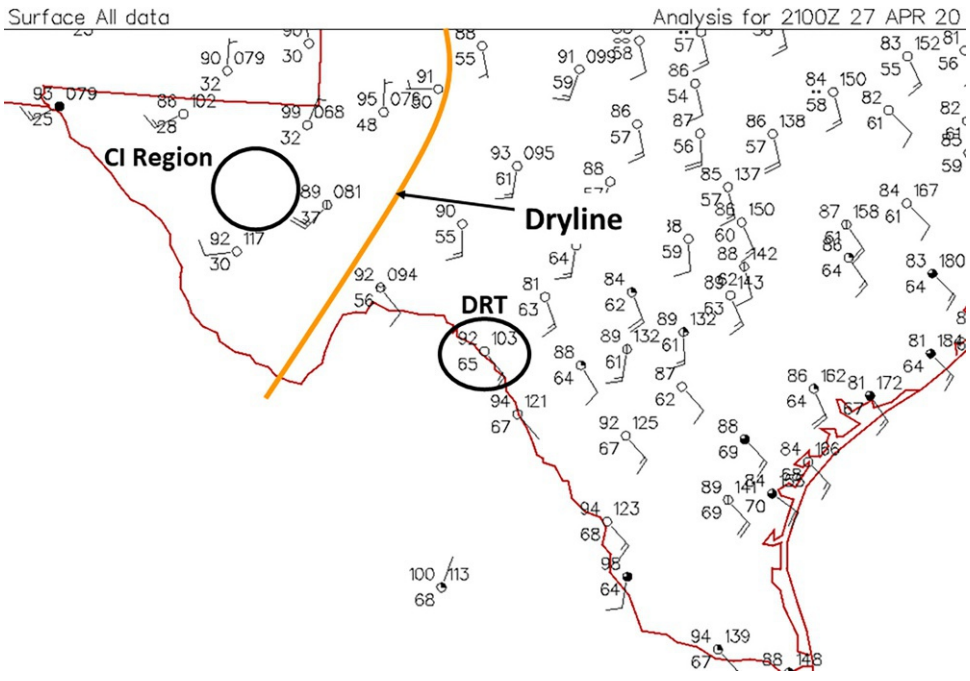

FIG. 2 Surface analysis over the southern Great Plains region at 2100 UTC 27 April 2020. The *black circled* region labeled "DRT" represents the location of the Del Rio, Texas and the location of the NOAA-20 sounding retrieval. "CI" represents the convective initiation region over the Davis Mountains of Texas. *(Courtesy of Plymouth State Weather Center.)*

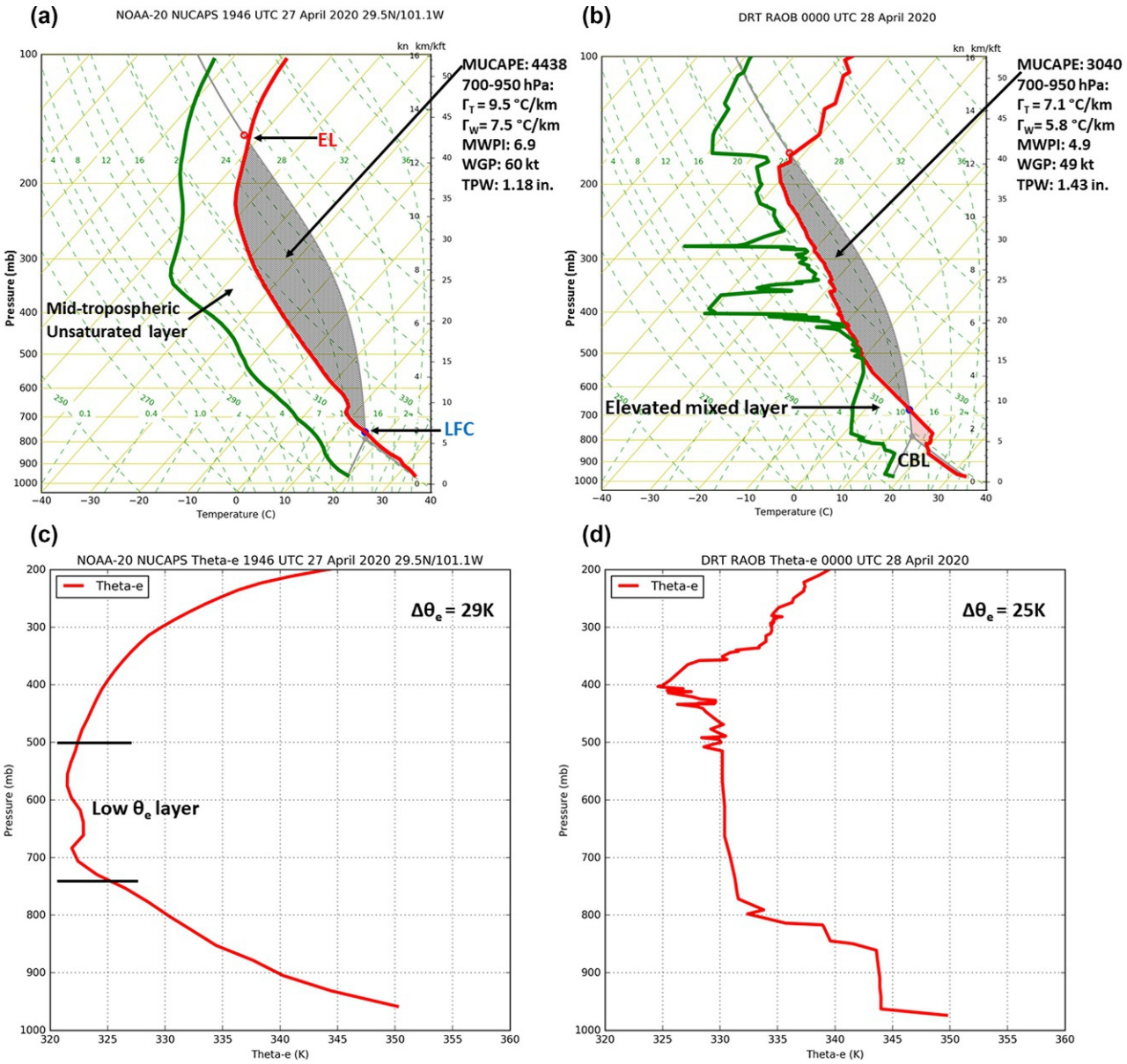

FIG. 3 (A) A NOAA-20 NUCAPS sounding profile retrieved during the afternoon of April 27, 2020, as compared to (B) a radiosonde observation at Del Rio, Texas (DRT) at 0000 UTC April 28, 2020; (C) A NOAA-20 NUCAPS theta-e profile retrieved during the afternoon of April 27, 2020, as compared to (D) a radiosonde observation theta-e profile at Del Rio, Texas (DRT) at 0000 UTC April 28, 2020. In (A) and (B), *red curves* and *green curves* represent the temperature and dewpoint soundings in degrees Celsius (°C), respectively. "MUCAPE" is most unstable parcel CAPE in J kg^{-1}, "MWPI" represents the Microburst Windspeed Potential Index (Pryor, 2015), "WGP" represents wind gust potential derived from the MWPI in knots (kt), and "TPW" represents total precipitable water in inches (in.). Γ_T and Γ_w represent dry-bulb temperature and wet-bulb temperature lapse rates, respectively.

MWPI value of 6.9 indicated thunderstorm wind gust potential of 60 knots. MWPI values greater than 5 indicate a high probability of severe winds greater than 50 knots in magnitude. In addition, the corresponding equivalent potential temperature (theta-e) profile signified potential instability with a decreasing value from the surface upward to a minimum in the middle troposphere. The calculated surface to 500 mb theta-e difference of 29 K (Fig. 3C) significantly exceeds the 20 K threshold for downburst occurrence as documented by Atkins and Wakimoto (1991). Comparing the 1945 UTC (2:45 pm local time) NUCAPS sounding profile (Fig. 3A), to the 0000 UTC (7:00 pm local time) 28 April RAOB from Del Rio (Fig. 3B), with a distance between retrieval locations of 22 km (12 n mi), shows that the risk for severe weather persisted into the evening.

Previous evaluations of NUCAPS for stability index calculation and convective weather forecasting applications (Bloch et al., 2019; Esmaili et al., 2020) described the necessity and resultant implementation of a modification technique to mitigate temperature and moisture biases in the boundary layer. This boundary layer correction replaces NUCAPS surface temperature and dewpoint temperature measurements with adjacent data from the Real Time Mesoscale Analysis (RTMA). The modification technique for the NUCAPS sounding profile in this case study, as shown in Fig. 4, was applied by adding the surface temperature and dew point measurements from Del Rio International Airport (DRT) to the retrieval. This procedure resulted in a stronger signal for severe outflow wind generation as evidenced by increased wind gust potential to 65 knots. Accordingly, the National Weather Service/Storm Prediction Center, in mesoscale discussion (MCD) #0481 issued at 2333 UTC 27 April, placed the Del Rio area in the southeastern periphery of a threat region for isolated strong/severe wind gusts (Fig. 5A). A Laughlin AFB NEXRAD reflectivity image highlighted the linear structure of the MCS with an array of protrusion echoes pointing downshear (Fig. 5B). This MCS likely generated a downburst cluster, resulting in wind gusts of 67 and 65 knots, recorded at Del Rio International Airport at 0135 UTC and at Laughlin Air Force Base at 0150 UTC 28 April, respectively. Calculated gust factors near 1.6 and ΔT values of -12 to -13°C for both wind events are consistent with downburst occurrence (Choi and Hidayat, 2002; Proctor, 1989). In addition, there was an unofficial report of a 90-knot wind gust from a personal weather station in the Del Rio area (D. Schreiber, Personal communication, April 30, 2020) as well as reports of major structural (i.e., roof) damage, uprooted trees, and power line and grid damage.

Defense Meteorological Satellite Program (DMSP) F-17 and MetOP-A overpasses were optimal for retrieving cloud microphysical properties before and shortly after the downburst in the Del Rio area, as inferred from TB measurements shown in Fig. 6. Imagery from Special Sensor Microwave Imager Sounder (SSMIS) and Microwave Humidity Sounder (MHS) displayed in Fig. 6 show remarkably cold cloud tops (white shading) and large graupel water path values (>1 mm) that indicated significant storm severity. As shown in Fig. 6A and B, the 91 GHz channel is an atmospheric window in the microwave spectrum. Scattering by ice-phase precipitation particles, especially graupel, hail, and snow above the freezing level, causes the TB depression (Ferraro et al., 2015; Laviola et al., 2020) around the time of peak storm intensity. For this case, TB near the storm centroid was remarkably low (~120 K) and corresponded to a maximum in graupel water path (GWP) values (>10 mm), indicating the presence of a dense core of graupel/hail. A large ice content and prominent dry-air notches on the lateral and downshear (forward) flanks of the storm indicated favorability for strong thunderstorm downdraft generation (Srivastava, 1987; Knupp, 1989). MetOP-A MHS imagery shown in Fig. 6C and D

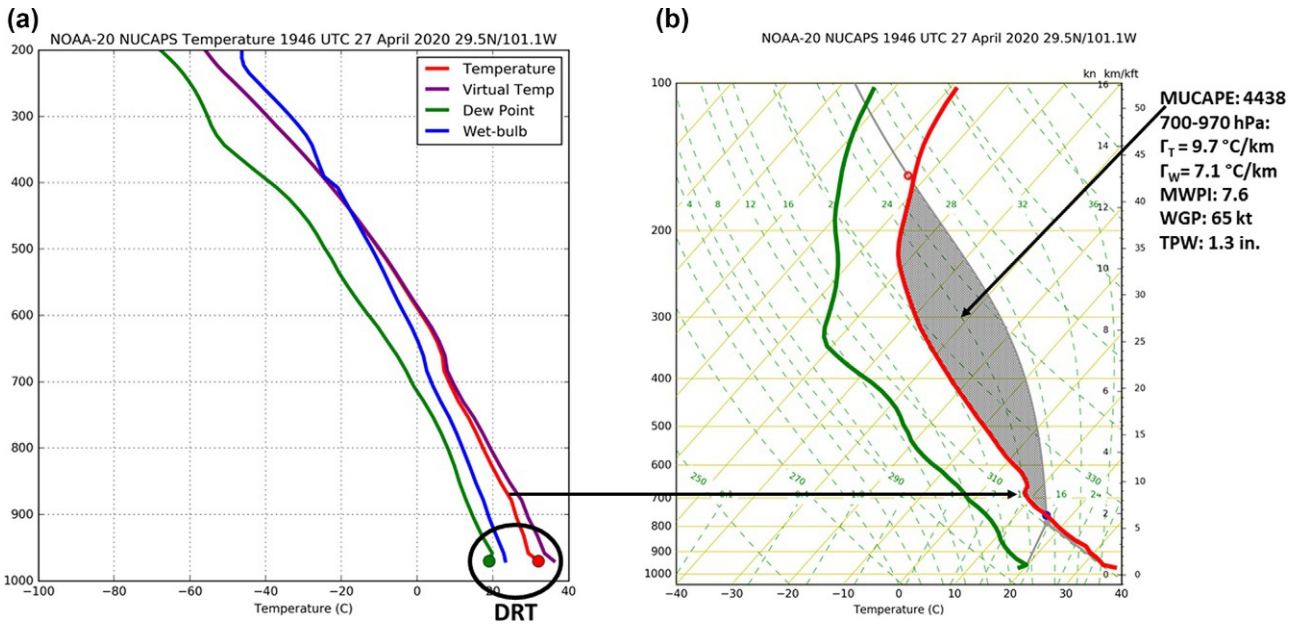

FIG. 4 (A) The NOAA-20 NUCAPS temperature sounding profile marked with surface observations of temperature and dew point retrieved at 1946 UTC near Del Rio, Texas (DRT); (B) corresponding sounding profile over Del Rio modified with the surface temperature and dew point observations at DRT. In (B), *red curves* and *green curves* represent the temperature and dewpoint soundings in degrees Celsius (°C), respectively. "MUCAPE" is most unstable parcel CAPE in J kg^{-1}, "MWPI" represents the Microburst Windspeed Potential Index (Pryor, 2015), "WGP" represents wind gust potential derived from the MWPI in knots (kt), and "TPW" represents total precipitable water in inches (in). Γ_T and Γ_w represent dry-bulb temperature and wet-bulb temperature lapse rates, respectively.

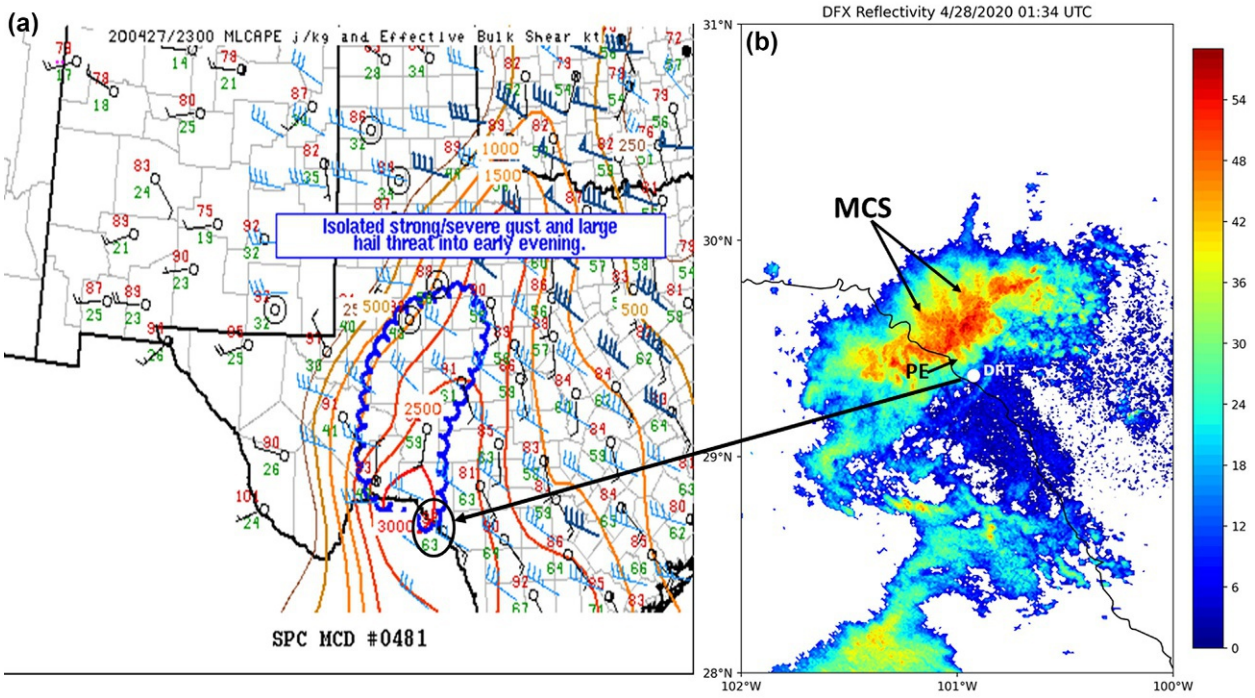

FIG. 5 (A) NWS/SPC mesoscale convective discussion (MCD) at 2300 UTC April 27, 2020. (B) Laughlin AFB, Texas NEXRAD reflectivity at 0134 UTC April 28, 2020. *Black-circled* region in (A) marks the location of Del Rio ("DRT"). "PE" represents the location of a protrusion echo.

displayed remarkably cold cloud tops (white shading) and large graupel water path values (>1 mm) that indicated significant storm severity.

This intensive study of a severe convective wind event demonstrates the value of a synergistic analysis of satellite and ground-based sensor data. This is illustrated by the afternoon NUCAPS vertical profile pointing to the potential for convection and verification by the appearance of severe convective storms in SSMIS and MHS imagery. Successive overpasses of DMSP F-17 and EPS MetOP-A satellites shown in Fig. 7 provided microwave imagery that effectively visualized the severe MCS evolution. Fig. 8 demonstrates the application of brightness temperature differencing to more effectively extract signatures associated with storm severity and intense convective downdraft generation. A new algorithm is the differential brightness temperature (BTDR) between the horizontal and vertical polarization channels that is analogous to Doppler radar-derived differential reflectivity:

$$\mathrm{BTDR} = 100^{*}(\log_{10}(TB91_H/TB91_V)) \tag{3}$$

where $TB91_H$ and $TB91_V$ represent horizontally and vertically polarized 91 GHz brightness temperatures, respectively. Small negative values of SSMIS-derived BTDR correspond to large graupel water path values (>10 mm), and thus to a mixture of rain, hail, and graupel. The calculation of BTDR is compared to the established polarization corrected temperature (PCT, Spencer et al. (1989)), defined as.

$$\mathrm{PCT} = \left(1.818^{*}TB_V\right) - \left(0.818^{*}TB_H\right) \tag{4}$$

where TB_H and TB_V represent horizontally and vertically polarized brightness temperatures, respectively. PCT values below 200 K typically correspond to high precipitation rates and large ice-phase precipitation content.

As shown in Fig. 9, the velocity azimuth display (VAD) wind profile (VWP) from Laughlin Air Force Base (AFB) NEXRAD, this multicellular storm tracked east-southeastward with weak low-level shear that was nearly parallel to the storm line, which allowed for a short episode of severe downburst winds over the Del Rio area, followed by gradual weakening of the system and cessation of severe winds. Also apparent were inward-directed V-shaped TB gradients on the downwind (eastern) flank of the storm that suggests the occurrence of wake entrainment of sub-saturated air and subsequent downdraft acceleration by the process detailed in Knupp (1989). The absence of an apparent rear-inflow jet was likely a

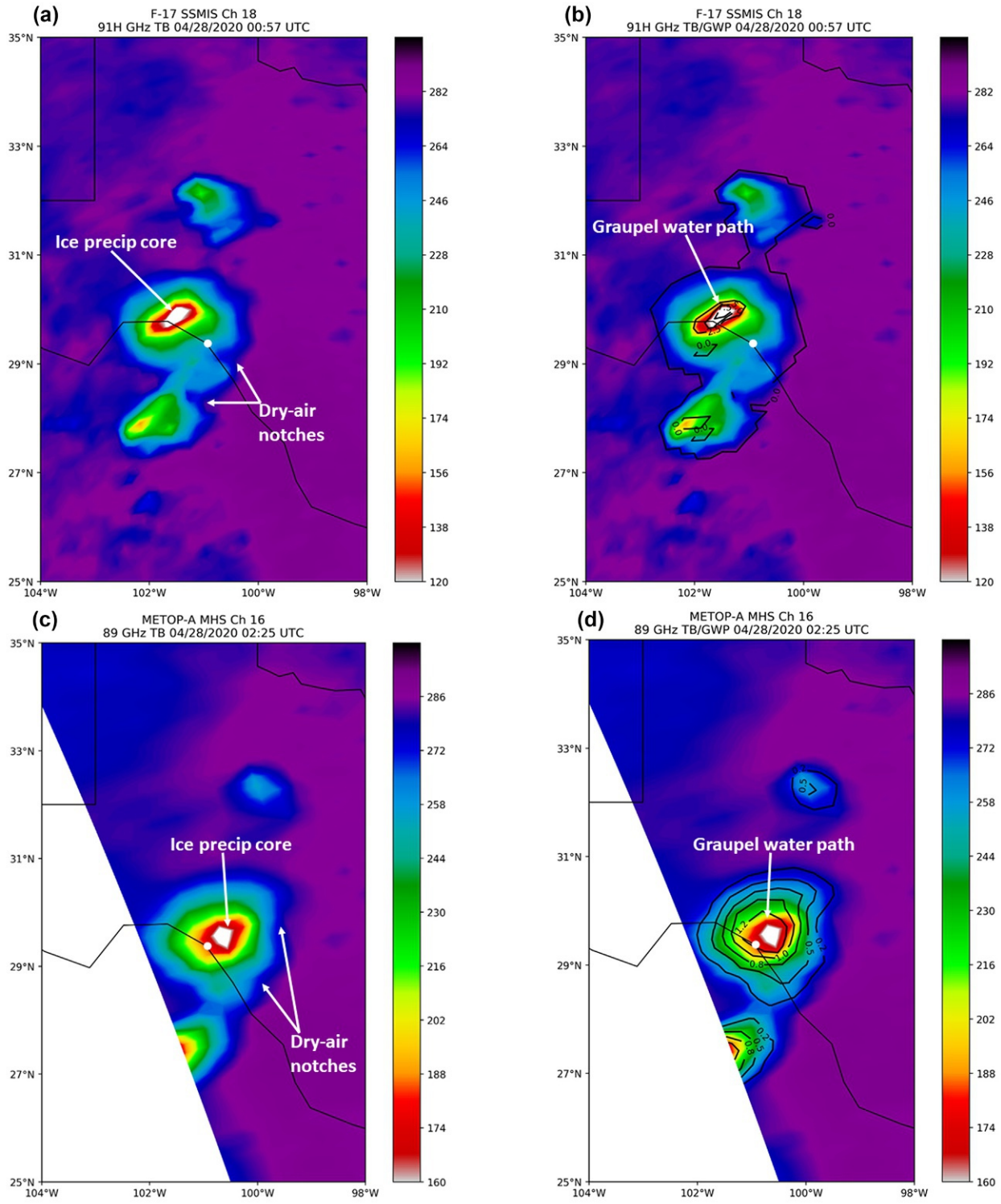

FIG. 6 South Texas Regional F-17 SSMIS (A) 91 GHz brightness temperature image at 0057 UTC April 28, 2020 with (B) overlying graupel water path ("GWP") measurements (in mm); (C) MetOP-A Microwave Humidity Sounder (MHS) 89 GHz brightness temperature image at 0225 UTC April 28, 2020 with (D) overlying graupel water path ("GWP") measurements (in mm). GWP contours are every 2.5 mm. *White circle* marks the location of Del Rio.

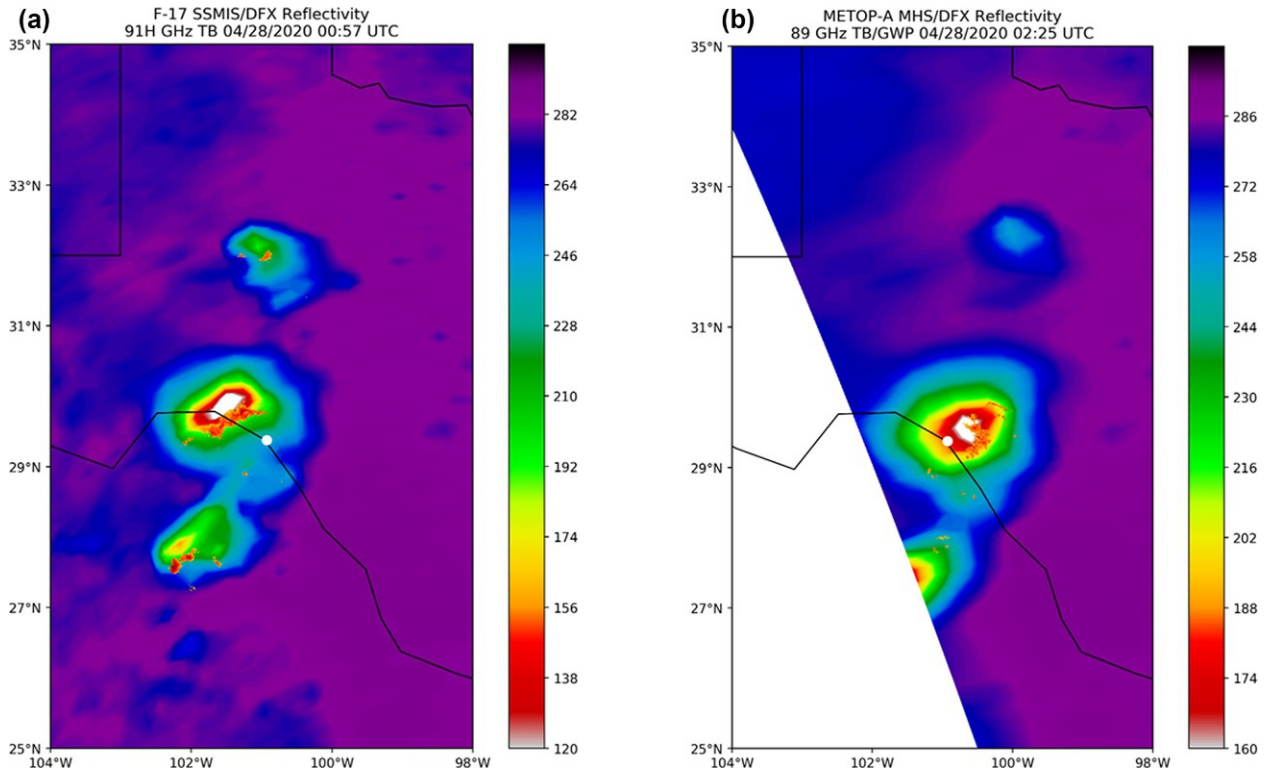

FIG. 7 South Texas Regional F-17 SSMIS (A) 91 GHz brightness temperature image at 0057 UTC April 28, 2020 and (B) MetOP-A MHS 89 GHz brightness temperature image at 0225 UTC April 28, 2020 with overlying NEXRAD reflectivity measurements (in dBZ). *White circle* marks the location of Del Rio.

factor in the episodic and short-lived occurrence of downburst winds at Del Rio with a duration only 15 min, from 0135 to 0150 UTC 28 April. However, these storms still produced significant structural damage and power outages on a local scale.

4.2 29 June 2012 North American derecho

During the morning of June 29, 2012, an area of convective storms over Iowa organized into a quasi-linear convective system (QLCS) as it tracked into northern Illinois. The system then evolved into a bow echo (Przybylinski, 1995) during the afternoon and tracked southeastward over the Ohio Valley to the Mid-Atlantic coast by late evening. What would eventually become the June 29, 2012, North American Derecho, this QLCS produced its first significant severe downburst, with winds measured over 65 knots, at Michigan City, Indiana during the early afternoon. This extraordinary derecho-producing convective system (DCS) event resulted in 22 deaths and nearly a thousand severe wind reports from northern Illinois to the Atlantic Coast. This system was more typical of a warm-season progressive derecho, as shown in Fig. 10, associated with a major heat wave and an elevated mixed layer (Banacos and Ekster, 2010). This DCS was generated and then propagated within a mid-tropospheric ridge synoptic pattern as identified by Johns (1993) and Coniglio et al. (2004). In addition, the derecho system maintained a type 2 echo pattern, as described by Przybylinski (1995), through most of its track through the Ohio Valley and Mid-Atlantic regions. The type 2 echo is characterized by "a short, solid bowing convective line segment of between 80 and 100 km in length. A band of scattered to broken convective elements is associated with a surface frontal boundary or warm advection zone and typically extends downwind (eastward) from the northern end of the bulging line echo" Przybylinski (1995). During the evening of 29 June, the derecho tracked rapidly eastward across the mountains of West Virginia (WV), western Virginia (VA), southwest Pennsylvania (PA), and western Maryland (MD) during mid-evening. The derecho's effects were particularly formidable in the Washington, DC–Baltimore, MD corridor, where measured wind gusts of 60–70 knots severed numerous overhead electrical feeders.

Comparison of the late evening MetOP-A Infrared Atmospheric Sounding Interferometer (IASI) sounding near Salisbury, Maryland to the HUBC microwave radiometer (MWR) sounding at 0200 UTC 30 June in Figs. 11 and 12 exhibits a transition to a moist and highly unstable profile favorable for severe wet microbursts. Fig. 11 illustrates the sounding

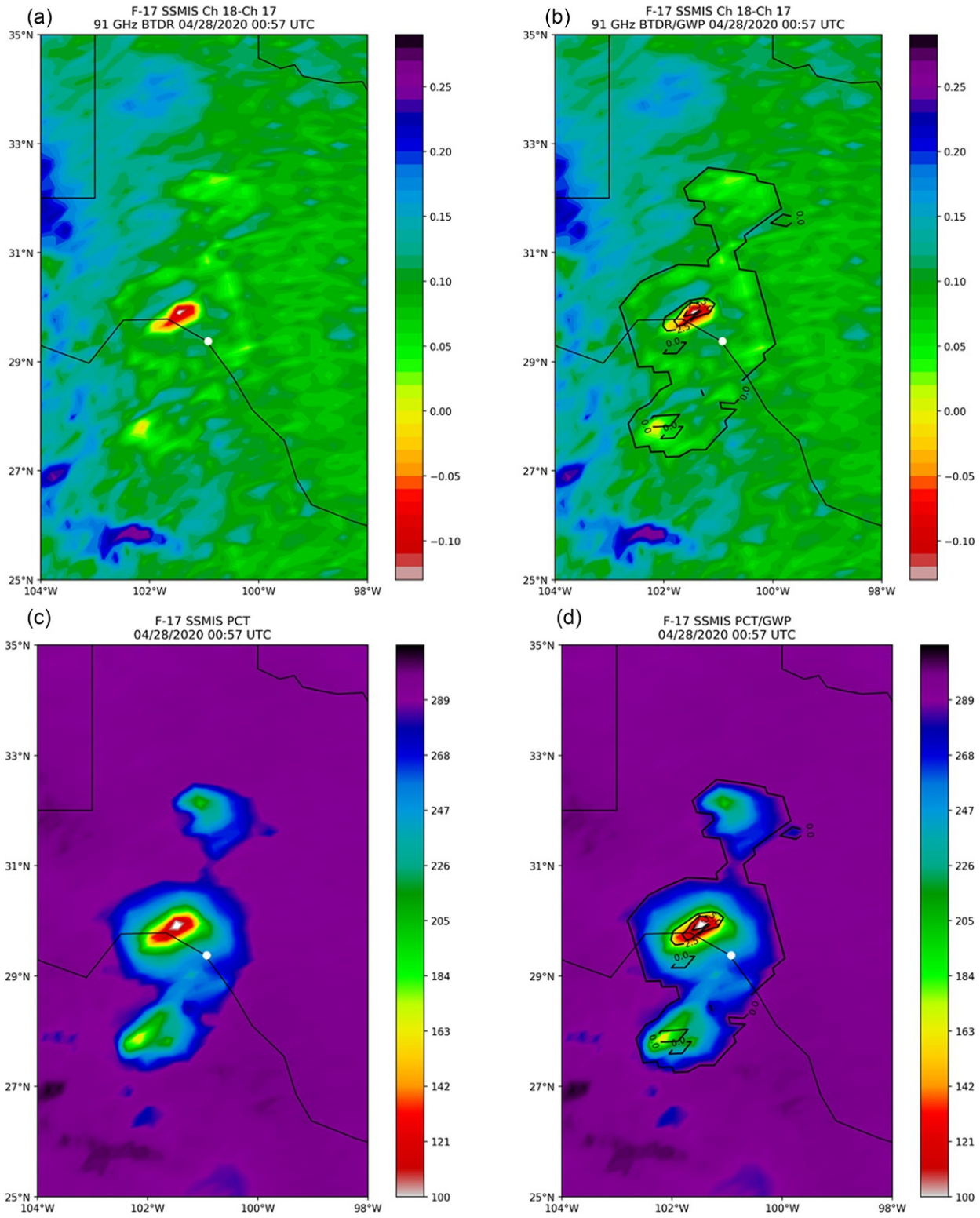

FIG. 8 F-17 SSMIS (A) differential brightness temperature (BTDR) imagery and (C) polarization corrected temperature (PCT) near 0100 UTC 28 April 2020. (B) and (D) display the product imagery with overlying graupel water path ("GWP", in mm). GWP contours are every 2.5 mm. *White circle* marks the location of Del Rio.

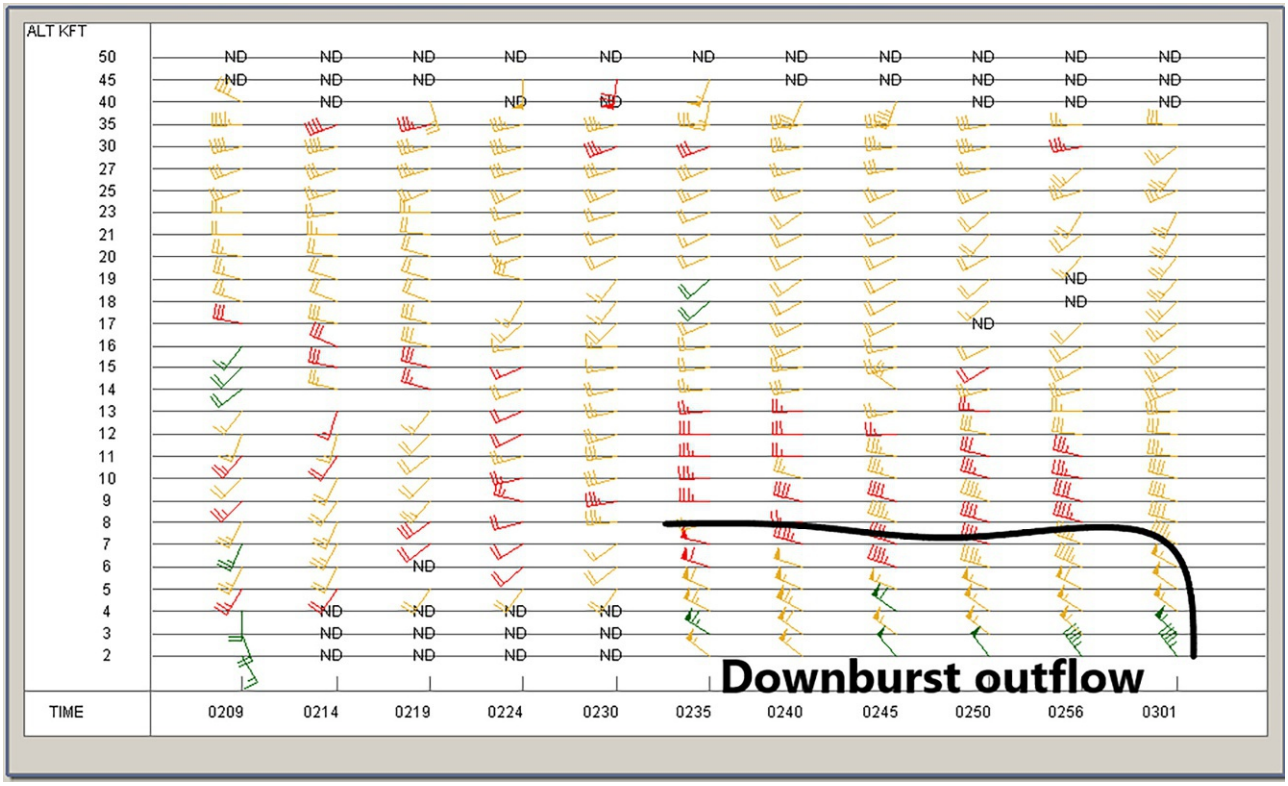

FIG. 9 Velocity azimuth display (VAD) wind profile (VWP) from Laughlin Air Force Base (AFB) NEXRAD, near Del Rio, Texas between 0200 and 0300 UTC April 28, 2020.

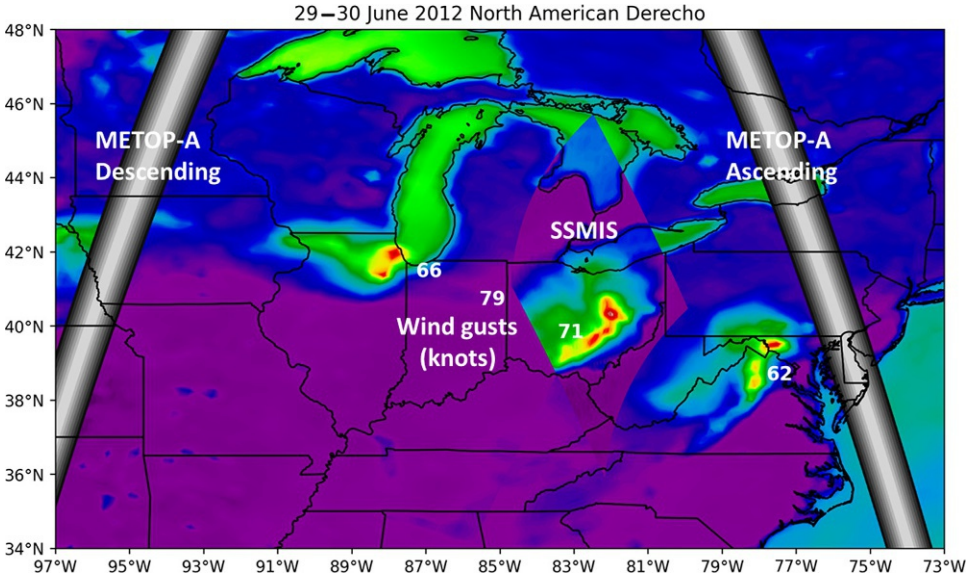

FIG. 10 Summary composite image of the June 2012 North American Derecho displaying the 29 June descending node and 30 June ascending node METOP-A orbit (nadir) tracks, MHS and SSMIS 89–91 GHz channel brightness temperature (TB, degrees Kelvin (K)) and significant wind reports (kt) along the storm track.

modification process to further enhance the signal for severe deep convective storm development. In Fig. 11A, the IASI thermodynamic profile indicated modest convective storm potential. Incorporating the 0154 UTC surface temperature and dew point observation from Salisbury Regional Airport (27 km (14 n mi) north of the IASI retrieval site), as shown in Fig. 11B, results in significantly larger CAPE. Finally, substituting the dry bulb temperature data set with calculated virtual temperature yields the strongest signal for severe downburst generation with wind gust potential of 57 knots, comparable to

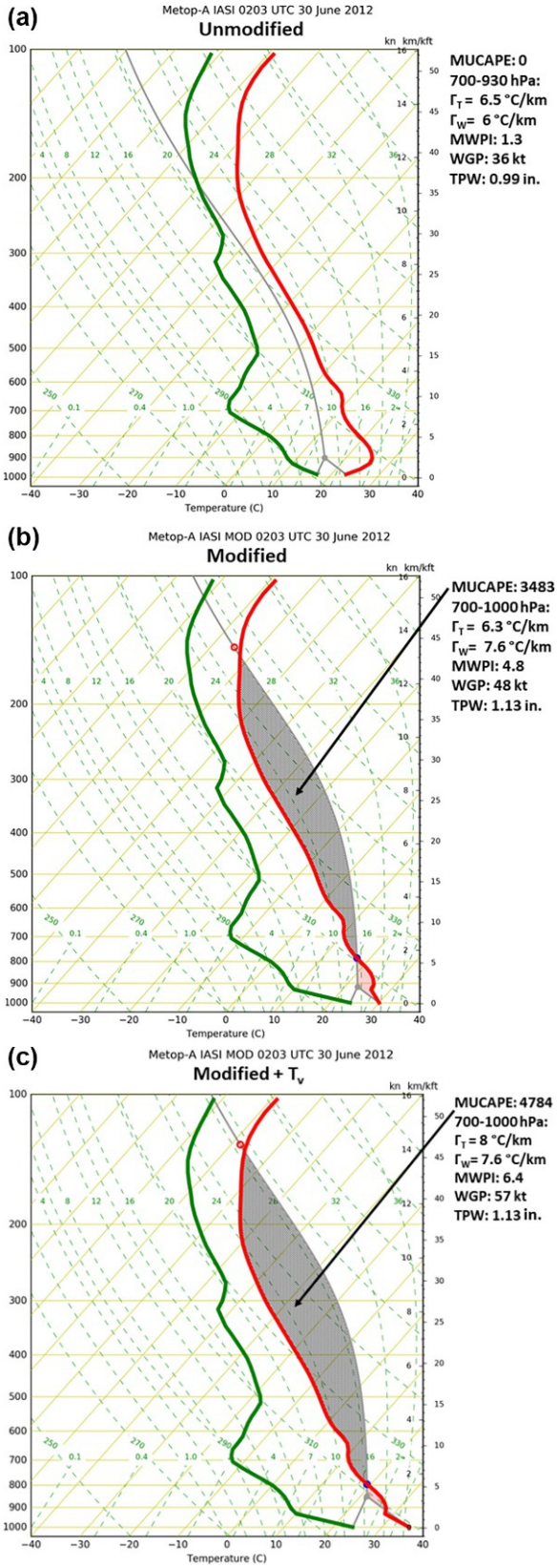

FIG. 11 MetOP-A IASI retrievals near Salisbury, Maryland during the evening of June 29, 2012 (0203 UTC 30 June): (A) IR + MW sounding profile; (B) IR + MW sounding profile modified by observed surface temperature and dew point at Salisbury Regional Airport; (C) modified IR + MW sounding profile plotted with virtual temperature. *Red curves* and *green curves* represent the temperature and dewpoint soundings in degrees Celsius (°C), respectively. "MUCAPE" is most unstable parcel CAPE in J kg^{-1}, "MWPI" represents the Microburst Windspeed Potential Index (Pryor, 2015), "WGP" represents wind gust potential derived from the MWPI in knots (kt), and "TPW" represents total precipitable water in inches (in). Γ_T and Γ_w represent dry-bulb temperature and wet-bulb temperature lapse rates, respectively.

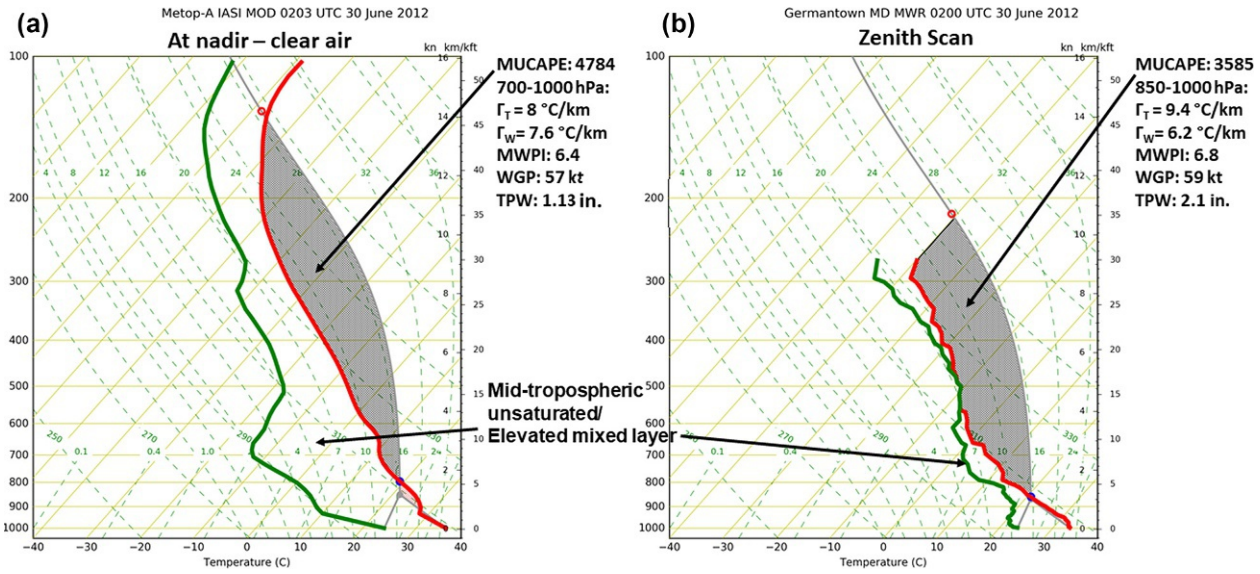

FIG. 12 (A) Modified MetOP-A IASI IR + MW sounding profile retrieved near Salisbury, Maryland at 0203 UTC June 30, 2012, as compared to (B) a ground-based sounding profile retrieval from the Germantown, Maryland microwave radiometer (MWR). *Red curves* and *green curves* represent the temperature and dewpoint soundings in degrees Celsius (°C), respectively. "MUCAPE" is most unstable parcel CAPE in J kg^{-1}, "MWPI" represents the Microburst Windspeed Potential Index (Pryor 2015), "WGP" represents wind gust potential derived from the MWPI in knots (kt), and "TPW" represents total precipitable water in inches (in). Γ_T and Γ_w represent dry-bulb temperature and wet-bulb temperature lapse rates, respectively.

the potential derived from the Germantown, Maryland MWR sounding as demonstrated in Figs. 11C and 12. Accordingly, the MWPI increased in magnitude prior to the onset of the derecho to eventually indicate convective wind gust potential of 57–59 knots with an hour of lead time. Since this author is not aware of routine use of this sounding modification technique in weather forecasting operations, the dissemination of this procedure to the operational meteorology community is paramount. The value added to the application of hyperspectral sounding analysis is demonstrated by the results of this technique. Between 0000 and 0200 UTC, as shown in Fig. 13, the DCS evolved into a double-bow echo pattern with a "warm advection wing" (Smith, 1990) over Frederick County (near latitude 39.5°N/longitude 77.4°W) that developed in an east-west oriented region of weak surface convergence over central Maryland.

Fig. 13 exhibits a type 2 derecho echo pattern with a warm advection wing (Przybylinski, 1995) that extended downwind (eastward) from the northern end of the bulging line echo. Microbursts occurred in Frederick County within the warm advection wing of the derecho. MetOP-A MHS, with overlying Sterling, VA (LWX) NEXRAD reflectivity, revealed the presence of the warm advection wing. A dry air notch, displayed as an inward (eastward) pointing TB gradient, likely indicated the presence of a rear-inflow jet ("RIJ") that sustained the MCS and the generation of downburst clusters in the DC-Baltimore corridor during the following hour. A shown in Figs. 14 and 15, the RIJ was apparent and distinguishable from surface-based outflow in the Sterling, Virginia NEXRAD VWP and Beltsville, Maryland 915 MHz Boundary Layer Profiler (BLP) wind observation time series, respectively. Near 0250 UTC, a downburst cluster tracking over downtown Washington, DC produced measured wind gusts of 61 and 47 knots at Reagan National Airport and the Washington Physical Oceanographic Real-Time System (PORTS) station, respectively. A gust factor of 1.42 and ΔT values of -10 to -11°C were also consistent with downburst occurrence embedded in the larger scale DCS.

In retrospect, NWS/Storm Prediction Center (SPC) adequately indicated the likelihood of scattered severe winds over the Washington, DC–Baltimore, MD corridor as the derecho tracked east of the Appalachian Mountains during the late evening. However, the density and magnitude of severe wind events, and associated impacts, over the Washington, DC metropolitan area, including the adjacent Maryland and Virginia suburbs, was not anticipated by neither SPC nor the NWS Office Baltimore-Washington. Furthermore, the MCD did not document any use of information from satellite-based sounding profilers or imagers, or ground-based profilers such as network MWRPs. Thus, science value added with this study of this derecho event entails the coordinated application of evening IASI and MWRP sounding profiles and derived parameters that will provide more insight into the evolution of the nocturnal convective lower troposphere. MW window channel data will more effectively interrogate evolving DCSs and reveal greater detail of storm structure, especially pertaining to convective wind generation. An important outcome of this study will be to formulate a correlation between MW parameters and signatures, and severe convective wind occurrence. The results of the evaluation of this derecho event

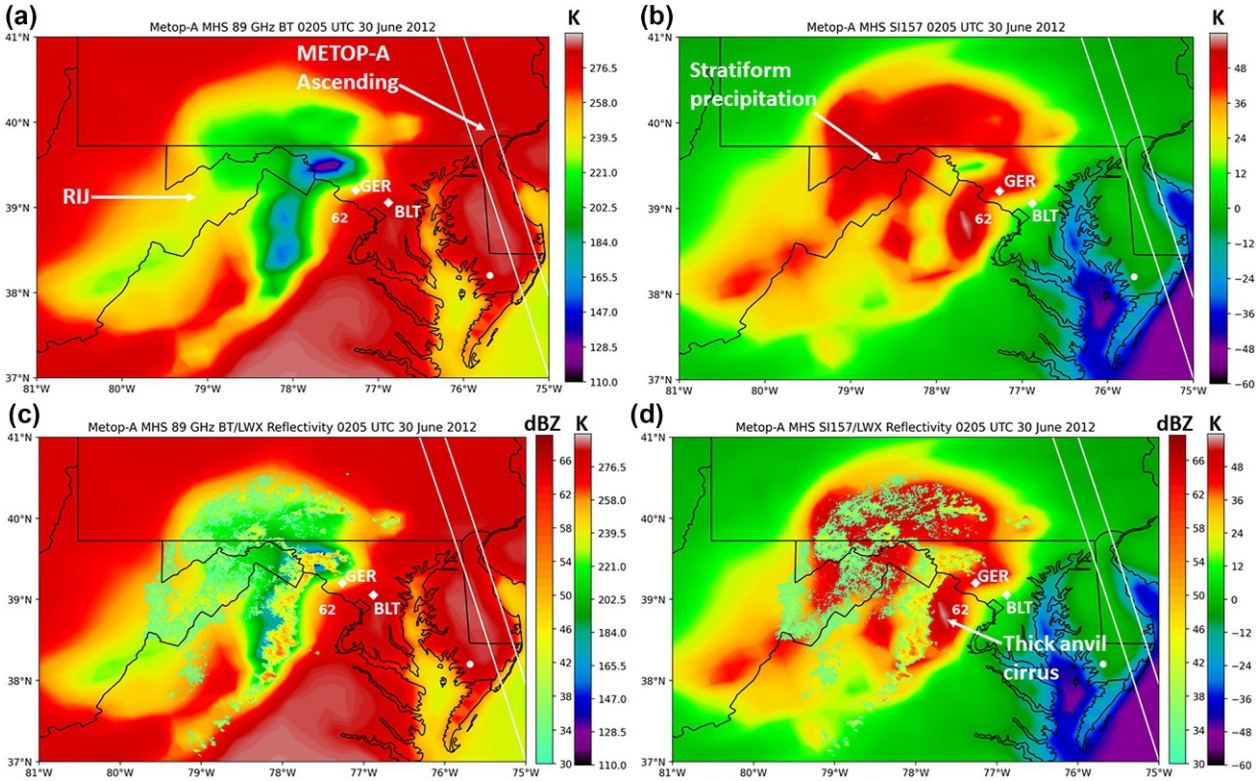

FIG. 13 METOP-A MHS 89 GHz brightness temperature (TB, K) image at 0200 UTC June 30, 2012 with (A) overlying Sterling, Virginia (LWX) NEXRAD radial velocity (kt) and (B) reflectivity (dBZ) measurements. (C, D) as in (A, B) with overlying Sterling, Virginia (LWX) NEXRAD reflectivity (dBZ) measurements. "GER" and "BLT" mark the location of the Germantown and Beltsville, Maryland MWRPs, respectively, The *white circle* marks the location of the IASI retrieval over Salisbury, Maryland, and "62" is the location of the first severe wind report in the Washington, DC metropolitan area (31.7 m s^{-1} (62 kt)) recorded at Dulles International Airport, Virginia. *White lines* mark the 30 June ascending node METOP-A orbit (nadir) tracks.

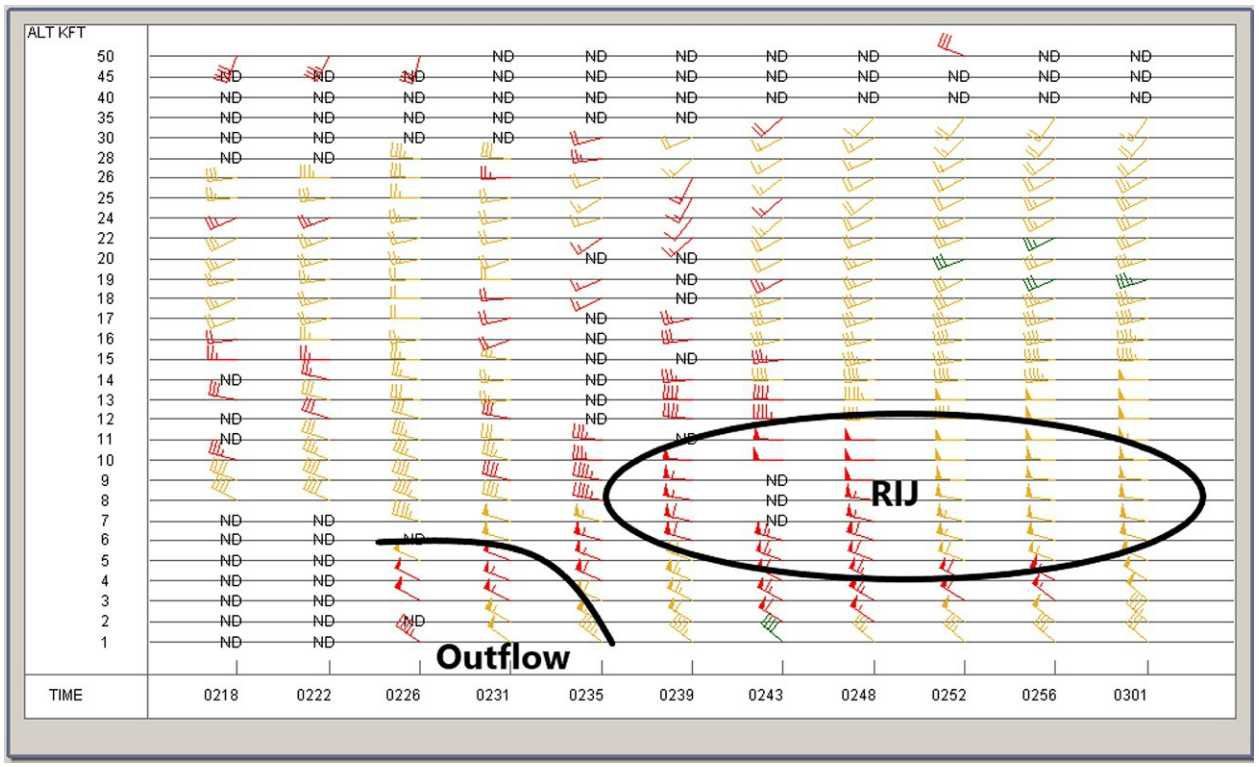

FIG. 14 Velocity azimuth display (VAD) wind profile (VWP) from Sterling, Virginia NEXRAD between 0200 and 0300 UTC June 30, 2012.

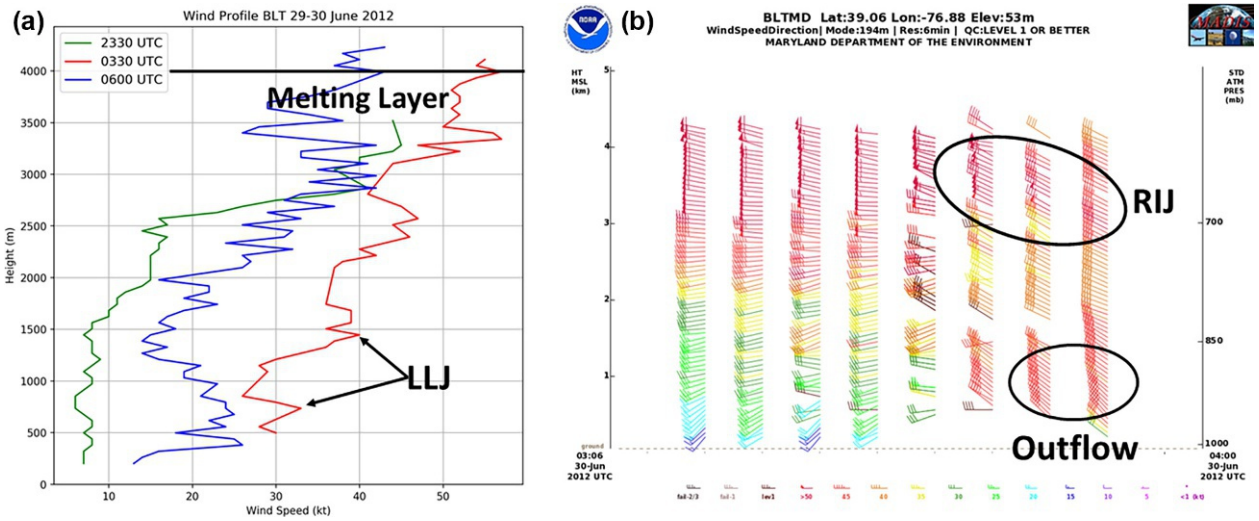

FIG. 15 Time series of HUBC 915 MHz Boundary Layer Profiler (BLP) (A) wind speed vs height (meters) between 2330 UTC 29 June and 0600 UTC June 30, 2012, and (B) wind speed and direction vs height between 0300 and 0400 UTC June 30, 2012.

necessitate the development and implementation of a nationwide NOAA ground-based microwave profiler network to provide the operational meteorology community near real-time access to high temporal resolution vertical temperature and moisture soundings.

5. Summary

Convective storm-generated downbursts are an operational forecasting challenge due to the spectrum of time, space, and intensity scales in which they occur. This chapter assembled the governing physical theory essential for development of downburst prediction algorithms that proceeds from vertical momentum equations and the aggregate of thermodynamical and microphysical processes of precipitation. Accordingly, downburst monitoring and subsequent prediction is a three-step process with an objective to build a three-dimensional model of the thermodynamic structure of the ambient environment and conceptual model of downburst-producing convective storms:

1. Collection and exploitation of surface-based observations including measurements from tower platforms and Doppler radar-measured reflectivity and wind velocity. This step promotes the enhanced use of the network of private and university-partnered ground-based MWRPs, as well as the archival of profiler datasets.
2. Ground-based microwave and radio profiler instruments, including MWRPs and BLPs, to obtain vertical profiles of temperature, humidity, and wind velocity. This step continues encouragement of algorithm development and multi-instrument synergistic interpretation of existing data assets.
3. Satellite-based 2-D plan view images of brightness temperature and vertical profiles of temperature and humidity. Modification of sounding profiles with surface observations of temperature and humidity is an additional step that results in improved representation of the ambient environment. Modifying sounding profiles with surface observations of temperature and humidity is an additional step that improves the representation of the ambient environment especially when performed with co-located MWRP sounding retrievals.

The case studies demonstrate how both ground-based and satellite-based observational data for convective storms can be combined for monitoring and forecasting applications. The strategic application of polar-orbiting meteorological satellite datasets and ground-based MWRP datasets allow for the comprehensive tracking of severe convective windstorms and DCSs through most of their lifecycles. With the advent of geostationary-satellite based hyperspectral infrared sounders, such as the InfraRed Sounder (IRS) to be deployed on Meteosat Third Generation (MTG) upon launch in 2024 (Iturbide-Sanchez et al., 2022), these observational techniques can be readily applied in near real-time to future convective windstorm events. With the expected improvement in humidity observations, the MTG IRS should satisfy a growing interest in severe convective windstorms that occur in Europe, in consideration of recent derecho events that impacted Germany in 2002 (Gatzen, 2004) and 2014 (Mathias et al., 2017). The IRS coverage area over the Atlantic Ocean, Europe, and Africa will suit preliminary assessment of this instrument in severe convective storm monitoring and prediction.

Passive microwave sounder imagery, as generated by low-Earth-orbit (LEO) satellite platforms, is vital for the inference of precipitation physical process and the resultant generation of convective outflow winds and confirms the hypothesis that convective windstorms are driven by unique aspects of the thermodynamic structure of the ambient environment and precipitation characteristics of the parent MCS. A challenge of the operational application of the derived microwave product imagery is the low temporal resolution (i.e., retrieval frequency) of LEO satellite passes over a region of interest, especially during the development phase of an MCS. Latency minimization procedures would mitigate a lower temporal resolution by providing derived products in near real-time to operational forecasting agencies. For MCSs with longer lifetimes (>6 h), successive overpasses with microwave image retrievals can effectively detect changes in storm intensity and the potential for widespread severe convective wind occurrence. The NASA Short-term Prediction Research and Transition (SPoRT) project disseminates microwave sounder imagery in near real-time through the web-based SPoRT Viewer (available online at https://weather.msfc.nasa.gov/sport/viewer/), which should serve as a benchmark to provide these products to operational weather forecasters. Field measurements are the cornerstone for remote sensing techniques and are essential for understanding deep convective storms and associated downburst occurrence, phenomena that encompass the vertical dimension of the troposphere.

Acknowledgments

The Author would like to acknowledge Rebekah Esmaili (STC) for reviewing the draft and providing constructive feedback. The author thanks Randolph Ware of Radiometrics Corporation for providing a comprehensive dataset of microwave radiometer profiles for analysis in this research effort and also thanks Dr. Belay Demoz of University of Maryland, Baltimore County, and Dr. Laurie Rokke of NOAA/NESDIS/STAR for their guidance and thorough internal review of the manuscript.

References

Ashley, W.S., Mote, T.L., 2005. Derecho hazards in the United States. Bull. Am. Meteorol. Soc. 86, 1577–1592.

Atkins, N.T., Wakimoto, R.M., 1991. Wet microburst activity over the southeastern United States: implications for forecasting. Weather Forecast. 6, 470–482.

Banacos, P.C., Ekster, M.L., 2010. The association of the elevated mixed layer with significant severe weather events in the Northeastern United States. Weather Forecast. 25, 1082–1102.

Bloch, C., Knuteson, R.O., Gambacorta, A., Nalli, N.R., Gartzke, J., Zhou, L., 2019. Near-real-time surface-based CAPE from merged hyperspectral IR satellite sounder and surface meteorological station data. J. Appl. Meteorol. Climatol. 58, 1613–1632.

Brock, F.V., Crawford, K.C., Elliott, R.L., Cuperus, G.W., Stadler, S.J., Johnson, H.L., Eilts, M.D., 1995. The Oklahoma Mesonet: a technical overview. J. Atmos. Oceanic Tech. 12, 5–19.

Bunkers, M.J., Klimowski, B.A., 2002. The importance of parcel choice and the measure of vertical wind shear in evaluating the convective environment. Preprints, 21st Conf. Severe Local Storms, San Antonio. Am. Meteorol. Soc. J117–J120, 11–16.

Choi, E.C., Hidayat, F.A., 2002. Gust factors for thunderstorm and non-thunderstorm winds. J. Wind Eng. Ind. Aerodyn. 90 (12–15), 1683–1696.

Cimini, D., Nelson, M., Güldner, J., Ware, R., 2015. Forecast indices from a ground-based microwave radiometer for operational meteorology. Atmos. Meas. Tech. 8 (1), 315–333.

Coniglio, M.C., Stensrud, D.J., Richman, M.B., 2004. An observational study of derecho-producing convective systems. Weather Forecast. 19, 320–337.

Ecklund, W.L., Carter, D.A., Balsley, B.B., 1988. A UHF wind profiler for the boundary layer: brief description and initial results. J. Atmos. Oceanic Tech. 5 (3), 432–441.

Ellrod, G.P., 1989. Environmental conditions associated with the Dallas microburst storm determined from satellite soundings. Weather Forecast. 4, 469–484.

Esmaili, R.B., Smith, N., Berndt, E.B., Dostalek, J.F., Kahn, B.H., White, K., Barnet, C.D., Sjoberg, W., Goldberg, M., 2020. Adapting satellite soundings for operational forecasting within the hazardous weather testbed. Remote Sens. (Basel) 12, 886. https://doi.org/10.3390/rs12050886.

Ferraro, R., Beauchamp, J., Cecil, D., Heymsfield, G., 2015. A prototype hail detection algorithm and hail climatology developed with the advanced microwave sounding unit (AMSU). Atmos. Res. 163, 24–35.

Ferraro, R.R., Kusselson, S.J., Colton, M., 1998. An introduction to passive microwave remote sensing and its applications to meteorological analysis and forecasting. Natl. Weather Dig. 22, 11–23.

Fujita, T.T., 1985. The Downburst, Microburst and Macroburst. Satellite and Mesometeorology Research Paper 210. University of Chicago. 122 pp.

Fujita, T.T., Wakimoto, R.M., 1981. Five scales of airflow associated with a series of downbursts on 16 July 1980. Mon. Weather Rev. 109, 1438–1456.

Gatzen, C., 2004. A derecho in Europe: Berlin, 10 July 2002. Weather Forecast. 19, 639–645. https://doi.org/10.1175/1520-0434(2004)019<0639:ADIEBJ>2.0.CO;2.

Iturbide-Sanchez, F., Wang, Z., Kalluri, S., Chen, Y., Lynch, E., Divakarla, M., Tan, C., Zhu, T., Cao, C., 2022. Exploration of a future NOAA infrared sounder in geostationary earth orbit. IEEE J. Sel. Top. Appl. Earth Observ. Remote Sens. 15, 1543–1561. https://doi.org/10.1109/JSTARS.2022.3142069.

Johns, R.H., 1993. Meteorological conditions associated with bow echo development in convective storms. Weather Forecast. 8, 294–299.

Knupp, K.R., 1989. Numerical simulation of low-level downdraft initiation within precipitating cumulonimbi: some preliminary results. Mon. Weather Rev. 117, 1517–1529.

Knupp, K.R., 1996. Structure and evolution of a long-lived, microburst producing storm. Mon. Weather Rev. 124, 2785–2806.

Laviola, S., Levizzani, V., Ferraro, R.R., Beauchamp, J., 2020. Hailstorm detection by satellite microwave radiometers. Remote Sens. (Basel) 12 (4), 621.

Liu, G., Curry, J.A., Sheu, R.W., 1995. Classification of clouds over the western equatorial Pacific Ocean using combined infrared and microwave satellite data. J. Geophys. Res. Atmos. 100 (D7), 13811–13826.

Martner, B.E., Wuertz, D.B., Stankov, B.B., Strauch, R.G., Westwater, E.R., Gage, K.S., Dabberdt, W.F., 1993. An evaluation of wind profiler, RASS, and microwave radiometer performance. Bull. Am. Meteorol. Soc. 74 (4), 599–614.

Mathias, L., Ermert, V., Kelemen, F.D., Ludwig, P., Pinto, J.G., 2017. Synoptic analysis and hindcast of an intense bow echo in Western Europe: the 9 June 2014 storm. Weather Forecast. 32, 1121–1141. https://doi.org/10.1175/WAF-D-16-0192.1.

Moller, A.R., 2001. Severe local storms forecasting. In: Doswell, C.A. (Ed.), Severe Convective Storms. 28. American Meteorological Society, Boston, MA, pp. 433–480.

Nalli, N.R., Tan, C., Warner, J., Divakarla, M., Gambacorta, A., Wilson, M., Zhu, T., Wang, T., Wei, Z., Pryor, K., Kalluri, S., Zhou, L., Sweeney, C., Baier, B.C., McKain, K., Wunch, D., Deutscher, N.M., Hase, F., Iraci, L.T., Kivi, R., Morino, I., Notholt, J., Ohyama, H., Pollard, D.F., Té, Y., Velazco, V.A., Warneke, T., Sussmann, R., Rettinger, M., 2020. Validation of carbon trace gas profile retrievals from the NOAA-unique combined atmospheric processing system for the cross-track infrared sounder. Remote Sens. (Basel) 12, 3245. https://doi.org/10.3390/rs12193245.

Proctor, F.H., 1989. Numerical simulations of an isolated microburst. Part II: sensitivity experiments. J. Atmos. Sci. 46, 2143–2165.

Pryor, K.L., 2015. Progress and developments of downburst prediction applications of GOES. Weather Forecast. 30, 1182–1200. https://doi.org/10.1175/WAF-D-14-00106.1.

Pryor, K.L., 2017. Advances in downburst monitoring and prediction with GOES-16. In: 17th Conference on Mesoscale Processes, San Diego, CA, Amer. Meteor. Soc. Paper No. 10.6.

Przybylinski, R.W., 1995. The bow echo. Observations, numerical simulations, and severe weather detection methods. Weather Forecast. 10, 203–218.

Schaefer, J.T., 1986. The Dryline. In: Ray, P.S. (Ed.), Mesoscale Meteorology and Forecasting. American Meteorological Society, pp. 549–572.

Schroeder, J.L., Burgett, W.S., Haynie, K.B., Sonmez, I., Skwira, G.D., Doggett, A.L., Lipe, J.W., 2005. The West Texas Mesonet: a technical overview. J. Atmos. Oceanic Tech. 22, 211–222.

Smith, B.E., 1990. Mesoscale structure of a derecho-producing convective system: the southern Great Plains storms of May 4 1989. In: Preprints, 16th Conf on Severe Local Storms, Kananaskis Park, AB, Canada, Amer. Meteor. Soc, pp. 428–433.

Smull, B.F., Houze Jr., R.A., 1987. Rear inflow in squall lines with trailing stratiform precipitation. Mon. Weather Rev. 115, 2869–2889.

Spencer, R.W., Goodman, H.M., Hood, R.E., 1989. Precipitation retrieval over land and ocean with the SSM/I: identification and characteristics of the scattering signal. J. Atmos. Oceanic Tech. 6 (2), 254–273.

Srivastava, R.C., 1985. A simple model of evaporatively driven downdraft: application to microburst downdraft. J. Atmos. Sci. 42 (10), 1004–1023. https://doi.org/10.1175/1520-0469(1985)042<1004:ASMOED>2.0.CO;2.

Srivastava, R.C., 1987. A model of intense downdrafts driven by the melting and evaporation of precipitation. J. Atmos. Sci. 44, 1752–1773.

Wakimoto, R.M., 1985. Forecasting dry microburst activity over the high plains. Mon. Weather Rev. 113, 1131–1143.

Weisman, M.L., 1992. The role of convectively generated rear inflow jets in the evolution of long-lived mesoconvective systems. J. Atmos. Sci. 49, 1826–1847.

Weisman, M.L., Klemp, J.B., Rotunno, R., 1988. Structure and evolution of numerically simulated squall lines. J. Atmos. Sci. 45, 1990–2013.

Westwater, E.R., Crewell, S., Matzler, C., 2005. Surface-based microwave and millimeter wave radiometric remote sensing of the troposphere: a tutorial. IEEE Geosci. Remote Sens. Soc. Newslett. 134, 16–33.

Ziegler, C.L., Lee, T.J., Pielke, R.A., 1997. Convective initiation at the Dryline: a modeling study. Mon. Weather Rev. 125, 1001–1026.